INTERNATIONAL JOURNAL FOR NUMERICAL METHODS IN FLUIDS
Int. J. Numer. Meth. Fluids 2002; **39**:783–797 (DOI: 10.1002/fld.329)

The use of LES subgrid-scale models for shock capturing

Nikolaus A. Adams

Institute of Fluid Dynamics, ETH Zürich, CH-8092 Zürich, Switzerland

SUMMARY

A method for modelling of flow discontinuities based on deconvolution with a relaxation regularization (DDM) is compared with an essentially non-oscillatory scheme (ENO) without further modelling and with a dynamic Smagorinsky subgrid-scale model (DSM). For the DDM approach, a sufficiently accurate representation of the filtered non-linear combination of discontinuous solution components which arise from the convection term is obtained by regularized deconvolution applied to the filtered solution. For stable integration the evolution equations are supplemented by a relaxation regularization based on a secondary filter operation and a relaxation parameter. We apply the above method to the generic test case of a two-dimensional solenoidal velocity fluctuation field interacting with a normal shock. The results demonstrate a good agreement of DDM with a reference computation, while DDM significantly reduces computational cost. Predictions with DDM are found to provide a more accurate representation of the shock–vorticity–wave interaction phenomena than that which can be accomplished using the ENO scheme with or without subgrid-scale model. Copyright © 2002 John Wiley & Sons, Ltd.

KEY WORDS: shock capturing; large-eddy simulation; deconvolution; subgrid-scale modelling; compressible flows

1. INTRODUCTION

For non-linear conservation laws the interaction of represented scales, i.e. scales which are supported on a given grid, with non-represented scales is essential to provide sufficient numerical-entropy dissipation in order to ensure that the solution of the filtered conservation law converges to the correct entropy solution for decreasing grid spacing, the filter-width being proportional to the grid spacing. This can be achieved by regularizing the filtered evolution equation with an additional term providing numerical-entropy dissipation such as the von Neumann–Richtmyer artificial diffusion [16] or the higher-order diffusion of Jameson *et al.* [8]. A standard regularization for the filtered conservation equations used in large-eddy simulation (LES) is a proper eddy-viscosity, e.g. the Smagorinsky model [13]. For a scalar equation the Smagorinsky model reduces to a von Neumann–Richtmyer artificial viscosity. The main effect of an eddy-viscosity regularization in LES is to provide a sufficient amount of energy dissipation [9, 10].

*Permanent address: N. A. Adams, Institute of Fluid Mechanics, Technical University of Dresden, D-01062 Dresden, Germany

Received October 2001
Revised December 2001

These observations suggest a relation between subgrid-scale models, which approach the closure problem from a physical point of view by incorporating into the model as many properties as possible known from the underlying conservation law and its solution, and numerical techniques which regularize the discretization of a conservation law in order to ensure convergence to the correct entropy solution. We note that it has been attempted successfully for some flow configurations and certain flow parameters to replace a subgrid-scale model entirely by the regularization provided by the underlying numerical method (usually a non-linear mechanism which in effect amounts to a locally adjusted artificial diffusion). In this case, the subgrid-scale model is linked to the truncation error of the discretization [4]. Detailed investigations of this approach by Garnier *et al.* [6] show, however, that it lacks general applicability. Two ways can be taken to close the link between physical and numerical subgrid-scale modelling. First, one can attempt to design the regularization of a non-linear numerical scheme such that its dominant truncation-error terms coincide with approximate subgrid-scale closures. Work following this direction will be reported elsewhere. Second, one can consider subgrid-scale models which were derived for turbulent flows and adapt them such that they provide a correct representation of filtered flow discontinuities.

In this paper we will contribute to the latter of these two approaches and compare three different subgrid-scale models for a generic test case for shock–turbulence interaction, where two-dimensional vorticity fluctuations interact with a shock wave. We compare the direct-deconvolution method (DDM) of Adams and Stolz [2], where a non-dissipative numerical discretization is used, with a monotonically integrated approach (MILES) using a third-order essentially non-oscillatory scheme (ENO) based on a Roe-flux formulation with entropy fix [19] and a dynamic Smagorinsky model with the ENO scheme as underlying discretization. The significance of subgrid-scale modelling with non-dissipative numerical discretizations is also supported by Ducros *et al.* [5] who have pointed out that spurious numerical diffusion away from shocks may affect the proper turbulence amplification when it interacts with the shock.

In Section 2 we detail the different approaches. In Section 3 we apply the subgrid-scale model to the full two-dimensional Euler equations on a finite domain where a shock interacts with an oblique vorticity wave.

2. SUBGRID-SCALE MODELLING

We consider a generic non-linear transport equation

$$\frac{\partial u}{\partial t}+\frac{\partial F_x(u)}{\partial x}+\frac{\partial F_y(u)}{\partial y}=0, \quad 0\leqslant x\leqslant L_x,\ \ 0\leqslant x\leqslant L_y \tag{1}$$

from which a filtered transport equation for the filtered variable $\bar{u}$

$$\frac{\partial \bar{u}}{\partial t}+\frac{\partial F_x(\bar{u})}{\partial x}+\frac{\partial F_y(\bar{u})}{\partial y}=\mathscr{G} \tag{2}$$

is obtained by convolution with a homogeneous filter

$$\bar{u}(x,y)=\int_{-\infty}^{+\infty}\int G_x(x-x')G_y(y-y')u(x',y')\,\mathrm{d}x'\,\mathrm{d}y'=G*u \tag{3}$$

where

$$\mathscr{G}=\frac{\partial F_x(\bar{u})}{\partial x}-G*\frac{\partial F_x(u)}{\partial x}+\frac{\partial F_y(\bar{u})}{\partial y}-G*\frac{\partial F_y(u)}{\partial y} \tag{4}$$

is an error term due to the filtering. Equation (2) is the modified differential equation for $\bar{u}$, the solution of which would be identical to the filtered solution of Equation (1) if $\mathscr{G}$ could be computed exactly.

In Section 3 we will consider as test case the two-dimensional Euler equations of gas dynamics which are given by Equation (1) with the solution $u:=\{\rho,\rho u,\rho v,E\}=\{\rho,m_x,m_y,E\}$, where $E:=p/(\kappa-1)+\rho(u^2+v^2)/2$. The flux vectors are given by

$$F_x:=\{m_x,m_x^2/\rho+p,m_xm_y/\rho,m_x(E+p)/\rho\} \tag{5a}$$

$$F_y:=\{m_y,m_xm_y/\rho,m_y^2/\rho+p,m_y(E+p)/\rho\} \tag{5b}$$

We state the equations here although the DDM approach applies equally also to other flux definitions, since the formulation of the MILES and DSM approaches depends on the flux definitions.

2.1. Direct deconvolution model—DDM

For the primary-filter operation we choose as kernel the Gauß function. In real space the one-dimensional filter kernel is defined as

$$G(x-x')=2\sqrt{\frac{2}{\pi}}\,\frac{1}{\Delta}\,e^{-8\frac{(x-x')^2}{\Delta^2}} \tag{6}$$

where Δ is the filter width. The two-dimensional filter kernels are generated from the one-dimensional filter kernel according to Equation (3). The Fourier transform of Equation (6) is given by

$$\hat{G}(\xi)=e^{-\left(\frac{\Delta\xi}{4\sqrt{2}}\right)^2} \tag{7}$$

Given constant grid spacings h_x and h_y in x- and y-directions respectively, in the following set the primary-filter width $\Delta=4h$ with $h=(h_x+h_y)/2$. As filter-cutoff wavenumber of the primary filter we set $\xi_C=\xi_N/2=\pi/(2h)$ for which $\hat{G}(\xi_C)=0.3$.

We require the discrete representations of the filter (Equation (6)) to resemble closely the transfer function (Equation (7)) of the analytic filter kernel. Unlike the continuous filter kernel itself, its discrete representation is band-limited to $|\xi|\leqslant\xi_N$. The transfer functions of a discretization of Equation (3) by standard quadrature formulas (trapezoidal rule or Simpson's rule, e.g.) usually exhibit a considerable error, in particular at wavenumbers close to ξ_N. A convenient way for a more accurate numerical representation is to use a Padé filter [12, 15]. We define a filter to be of order m if the first non-vanishing derivative of its transfer function (its Fourier transform) is of order m at $\xi=0$. Let $\mathbf{f}$ be an $(N+1)$ vector containing the values of the grid function $f_i=f(x_i)$ obtained by sampling a continuous function $f(x)$ at a set of equally spaced nodes $x_j=x_0+jh$, $0\leqslant j\leqslant N$. Let $\bar{\mathbf{f}}$ denote the vector of filtered values obtained

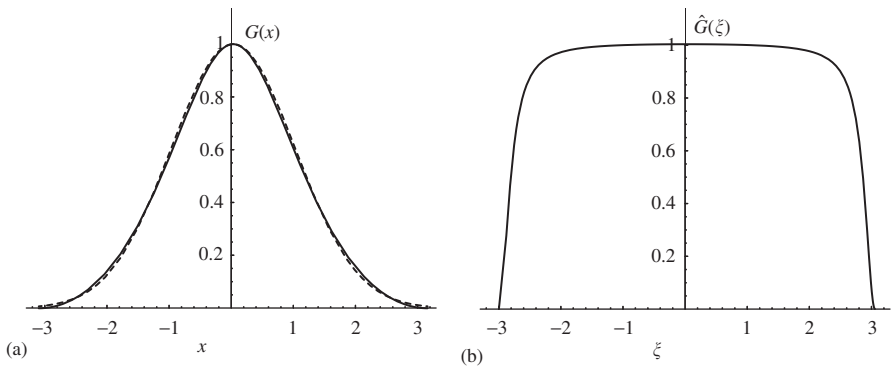

Figure 1. (a) Primary-filter kernel transfer function (Equation (6)) with $\Delta = 4h$, $h = 1$ - - - -, discrete primary filter (Equation (8)) with $\alpha = -0.2$ —-; (b) secondary-filter kernel transfer function.

by applying the discrete filter $\mathbf{G}$ to $\mathbf{f}$, in matrix-vector notation $\bar{\mathbf{f}} = \mathbf{G}\mathbf{f}$. Here, we consider the special case in which $\mathbf{G} = \mathbf{M}_l^{-1}\mathbf{M}_r$, and $\mathbf{M}_l$, $\mathbf{M}_r$ are tridiagonal matrices. A one-parameter family of filters with $m = 2$ is given by

$$\alpha \bar{f}_{j-1} + \bar{f}_j + \alpha \bar{f}_{j+1} = a f_j + \frac{b}{2}(f_{j-1} + f_{j+1}) \tag{8}$$

where $a = (1/2 + \alpha)$ and $b = a$. For a finite domain various treatments are possible at the boundary points $j = 0$ and $j = N$. We will in general impose no filtering at domain-boundary points. The kernel of a Gauß filter (Equation (6)) with filter width $\Delta = 4h$ is well approximated in Fourier space if one chooses $\alpha = -0.2$, Figure 1(a).

By a relation given by Pruett and Adams [15] the parameter α of Equation (8) can be linked to ξ_{C_2}. If the discrete-filter parameter is chosen as $\alpha = 0.49$ we obtain a secondary filter G_2 with $\xi_{C_2} = 0.958\pi$ for $\hat{G}_2(\xi_{C_2}) = 0.3$. The transfer function of the secondary one-dimensional filter kernel is shown in Figure 1(b). In the following we will call G_N and G_{2N} the discrete approximations of the corresponding continuous filters G and G_2, respectively.

Subgrid-scale modelling consists in two parts: (i) approximation of the error term $\mathscr{G}$ in Equation (2) involving the represented scales $|\xi| \leqslant \xi_N$, and (ii) construction of an appropriate regularization $\mathscr{R}$ in Equation (2) which models the effect of interaction between the non-represented scales $|\xi| > \xi_N$ and the resolved scales $|\xi| \leqslant \xi_C$. This split can be cast into two contributions, $\mathscr{G} \simeq \mathscr{G}_1 + \mathscr{R}$. The first term $\mathscr{G}_1$ can be computed exactly if the filter operation with the kernel G_N is invertible on the restriction of its domain to all bandlimited functions $u_N(x)$ with wavenumbers $|\xi| \leqslant \xi_N$ or grid functions with grid spacing $h = \pi/\xi_N$. Following this idea the direct-deconvolution method (DDM) for shock-capturing was developed by Adams and Stolz [2].

Since $\hat{G}_N(\xi)$ has compact support it is not invertible in general. If we, however, restrict the domain of $\bar{u}_N = G_N * u_N$ to bandlimited functions or grid functions with wavenumbers $|\xi| \leqslant \xi_N$, then an inverse exists, provided $\hat{G}_N(\xi) > 0$ on $|\xi| \leqslant \xi_N$. The transfer function of the primary filter kernel vanishes at $|\xi| = \xi_N$ and a regularized inverse can be constructed on unbounded domains by a singular-value decomposition where the vanishing eigenvalue is removed. The

approximate inverse is defined in Fourier dual space as

$$\hat{Q}_N = \begin{cases} \hat{G}_N^{-1}(\xi), & |\xi| < \xi_N \\ 0, & |\xi| = \xi_N \end{cases} \tag{9}$$

On bounded non-periodic domains an inverse of the discrete filter G_N exists if no filtering is imposed at the boundaries. In this case the spectrum of G_N is bounded away from zero on the positive real axis. For symmetric filters the eigenvalues of $\mathbf{G}$ are real.

Given a regularized inverse of the filtering operation, the term $\mathscr{G}_1$ can be approximated by replacing the unfiltered quantities in $F(u_N)$ with $\tilde{u}_N = Q_N * \bar{u}_N$ and solving the following evolution equation for $\bar{u}_N$:

$$\frac{\partial \bar{u}_N}{\partial t} + G_N * \frac{\partial F_x(\tilde{u}_N)}{\partial x} + G_N * \frac{\partial F_y(\tilde{u}_N)}{\partial y} = 0 \tag{10}$$

If the inversion is exact $Q_N * G_N = I$ we can write Equation (10) also as

$$G_N * \left(\frac{\partial u_N}{\partial t} + \frac{\partial F_x(u_N)}{\partial x} + \frac{\partial F_y(u_N)}{\partial y} \right) = 0 \tag{11}$$

A solution u_N of this equation without proper regularization fails to satisfy the entropy condition for admissible weak solutions [23]. In order to introduce numerical-entropy dissipation Equation (10) requires regularization. We construct a regularization based on a relaxation term which employs a secondary filter operation

$$\mathscr{R} = -\chi(\bar{u}_N - G_{2N} * \bar{u}_N) \tag{12}$$

where $\chi > 0$ is the inverse of some relaxation-time parameter and G_{2N} is a secondary filter of deconvolution type Equation (3), to the right-hand side of Equation (10). The advantage of relaxation regularizations is that they leave the type of the underlying differential equation unchanged since they constitute a lower order perturbation and do not affect its well-posedness [7]. Adams and Stolz [2] have demonstrated that χ can be estimated by an expression

$$\chi = C_0 + \frac{C_1}{h} \tag{13}$$

where C_0 and C_1 are constants determined by the initial condition.

2.2. *Monotonically integrated LES—MILES*

The acronym MILES, for monotonically integrated LES, commonly describes the situation if instead of employing an explicit subgrid-scale model the effect of the interaction of non-represented with resolved scales is modelled by the implicit regularization originating from the non-linearly stable numerical discretization. This involves usually monotonicity-preserving schemes, total-variation diminishing schemes, or the less restrictive essentially non-oscillatory schemes (ENO). In the terminology of Section 2.1 this amounts to $\mathscr{G}_1 = 0$ and $\mathscr{R}$ being replaced by the implicit regularization provided by the numerical discretization.

We follow Shu and Osher [19] with minor differences only in the implementation. Referring to Figure 2, the numerical flux vector at the cell centres $\hat{f}_{j+1/2}$ is calculated in the following

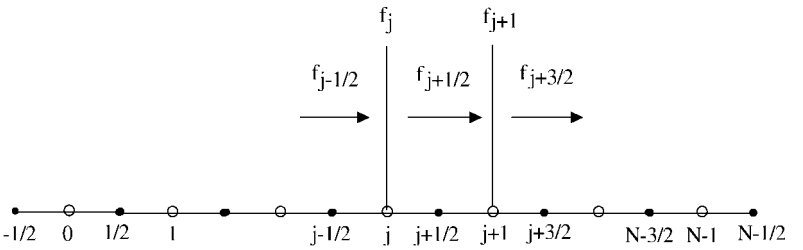

Figure 2. Grid function and fluxes for ENO scheme.

manner. Define

$$\kappa(j,k)=\sum_{v=0}^{k}\prod_{\substack{\mu=j\\ \mu\neq j+v}}^{j+k}(1-\mu),\quad k=0,\ldots,r-1,\ \ j=-r,\ldots,1 \tag{14}$$

The numerical fluxes at the cell centre $j+1/2$ are then obtained by

$$\hat{f}_{j+\frac{1}{2}}=\sum_{m=0}^{r}\kappa(i^{(m)}-j,m)\bar{A}_{j+\frac{1}{2}}\Delta_{i,m}[\bar{A}^{-1}_{j+\frac{1}{2}}f] \tag{15}$$

where $\bar{A}_{j+1/2}$ stands for the Roe matrix at $j+1/2$ [17]. With r we denote the order of the ENO scheme, which has accordingly $r+1$ levels. For the definition of the operator $\Delta_{i,m}$ and the flux vector f we have to distinguish two cases depending on Λ, the diagonal transform of $\partial F/\partial u$:

(a) For cell $j+\frac{1}{2}$, if $\lambda_j<0<\lambda_{j+1}$ then a Roe flux formulation may violate an entropy condition. In this case a local Lax–Friedrichs flux formulation is used and we define

$$f^{\pm}=\frac{1}{2}\left(F\pm\max_{j,j+1}|\Lambda|u\right) \tag{16}$$

and recursively

$$\Delta^{\pm}_{i^{(m)},m}=\begin{cases} f^{\pm}[i^{(m-1)},m], & i^{(m)}=i^{(m-1)}-1\\ & \text{if } |f^{\pm}[i^{(m-1)},m]|\leqslant|f^{\pm}[i^{(m-1)}+1,m]|\\ f^{\pm}[i^{(m-1)+1},m], & i^{(m)}=i^{(m-1)}\\ & \text{if } |f^{\pm}[i^{(m-1)},m]|>|f^{\pm}[i^{(m-1)}+1,m]| \end{cases} \tag{17}$$

for $m=0,\ldots,r$ and $i^{(0)}=j$ for Δ^{+} and $i^{(0)}=j+1$ for Δ^{-}. And finally it is

$$\Delta_{i,m}=\Delta^{+}_{i^{(m)},m}+\Delta^{-}_{i^{(m)},m} \tag{18}$$

(b) In case the former condition does not hold the less dissipative Roe flux formulation is used and we define

$$f=F \tag{19}$$

and recursively

$$\Delta_{i^{(m)},m} = \begin{cases} f[i^{(m-1)}, m], & i^{(m)} = i^{(m-1)} - 1 \\ & \text{if } |f[i^{(m-1)}, m]| \leqslant |f[i^{(m-1)} + 1, m]| \\ f[i^{(m-1)+1}, m], & i^{(m)} = i^{(m-1)} \\ & \text{if } |f[i^{(m-1)}, m]| > |f[i^{(m-1)} + 1, m]| \end{cases} \tag{20}$$

for $m = 0, \ldots, r$ and $i^{(0)} = j$, if $\bar{\lambda}_{j+1/2} \geqslant 0$ and $i^{(0)} = j + 1$ if $\bar{\lambda}_{j+1/2} < 0$.

The flux derivatives at the cell faces are reconstructed by

$$(\partial_x \hat{f})_j = \frac{1}{h}\left(\hat{f}_{j+\frac{1}{2}} - \hat{f}_{j-\frac{1}{2}}\right) \tag{21}$$

In Section 3 we will employ the 3rd order form of this ENO scheme. For two space dimensions, the flux in each coordinate direction is treated by the one-dimensional ENO procedure.

2.3. Dynamic Smagorinsky model—DSM

In terms of the filtered conservative variables $\bar{u} = \{\bar{\rho}, \bar{m}_x, \bar{m}_y, \bar{E}\}$ the continuity equation does not contain non-linearities and remains unchanged

$$\partial_t \bar{\rho} + \partial_x \bar{m}_x + \partial_y \bar{m}_y = 0 \tag{22a}$$

The momentum equations contain explicitly modelled subgrid-scale stress contributions $\tau_{xx}, \tau_{xy}, \tau_{yy}$

$$\partial_t \bar{m}_x + \partial_x \left(\frac{\bar{m}_x^2}{\bar{\rho}} + \mathscr{P}\right) + \partial_y \frac{\bar{m}_x \bar{m}_y}{\bar{\rho}} = \partial_x \tau_{xx} + \partial_y \tau_{xy} \tag{22b}$$

$$\partial_t \bar{m}_y + \partial_x \frac{\bar{m}_x \bar{m}_y}{\bar{\rho}} + \partial_y \left(\frac{\bar{m}_y^2}{\bar{\rho}} + \mathscr{P}\right) = \partial_x \tau_{xy} + \partial_y \tau_{yy} \tag{22c}$$

The energy equation is modelled as

$$\begin{aligned} &\partial_t \bar{E} + \partial_x \left(\frac{\bar{m}_x}{\bar{\rho}} (\bar{E} + \mathscr{P})\right) + \partial_y \left(\frac{\bar{m}_y}{\bar{\rho}} (\bar{E} + \mathscr{P})\right) \\ &= \frac{\bar{m}_x}{\bar{\rho}} (\partial_x \tau_{xx} + \partial_y \tau_{xy}) + \frac{\bar{m}_y}{\bar{\rho}} (\partial_x \tau_{xy} + \partial_y \tau_{yy}) + \partial_x \mathscr{Q}_x + \partial_y \mathscr{Q}_y \end{aligned} \tag{22d}$$

For the resolved pressure we use the abbreviation

$$\mathscr{P} = \left(\bar{E} - \frac{1}{2\bar{\rho}}(\bar{m}_x^2 + \bar{m}_y^2)\right)(\gamma - 1) \tag{23}$$

The subgrid-scale stresses are modelled according to Moin *et al.* [14], Vreman [25], as

$$\tau_{ij} = \bar{\rho} C_d \Delta^2 \|S\| S_{ij} \tag{24}$$

where ij is a placeholder for the combinations of x and y, S_{ij} is the trace-free strain tensor

$$S_{ij} = \partial_i \frac{\bar{m}_j}{\bar{\rho}} + \partial_j \frac{\bar{m}_i}{\bar{\rho}} - \delta_{ij} \partial_k \frac{\bar{m}_k}{\bar{\rho}} \tag{25}$$

and $\|S\|$ is the matrix-norm of S_{ij}

$$\|S\| = \sqrt{S_{xx}^2/2 + S_{xy}^2 + S_{yy}^2/2} \tag{26}$$

The isotropic part of the subgrid-scale stress tensor is neglected. Solutions for the problem in Section 3 incorporating this term did not show improved results. For the dynamic estimation of the Smagorinsky parameter C_d we need the Leonard-stress tensor

$$L_{ij} = \frac{\hat{\bar{m}}_i \hat{\bar{m}}_j}{\hat{\bar{\rho}}} - \left(\frac{\widehat{\bar{m}_i \bar{m}_j}}{\bar{\rho}} \right) \tag{27}$$

and the test-filtered subgrid-scale stresses, where the test-filter width is twice the primary-filter width

$$T_{ij} = \hat{\bar{\rho}} 4\Delta^2 \|\hat{S}\| \hat{S}_{ij} - \Delta^2 (\bar{\rho} \widehat{\|S\| S_{ij}}) \tag{28}$$

$\hat{S}_{ij}$ is S_{ij} evaluated with the test-filtered solution. The Smagorinsky parameter is determined from the contraction

$$C_d = \frac{T_{ij} L_{ij}}{T_{ij} T_{ij}} \tag{29}$$

where summation is performed over repeated place holders. For the computational results in Section 3 we have restricted (clipped) the values of the Smagorinsky parameter to remain in the range $C_d \in [0.05, 0.2]$, otherwise the computation was unstable.

The subgrid-scale heat flux $\mathcal{Q}$ is modelled as

$$\mathcal{Q} = \partial_x \frac{\bar{\rho} C_d \Delta^2 \|S\|}{(\gamma - 1) Pr_t M^2} \partial_x \mathcal{T} + \partial_y \frac{\bar{\rho} C_d \Delta^2 \|S\|}{(\gamma - 1) Pr_t M^2} \partial_y \mathcal{T} \tag{30}$$

$\mathcal{T} = \gamma M^2 \mathcal{P}/\bar{\rho}$, where we assume for simplicity a constant turbulent Prandtl number $Pr_t = 1$. Since for stable integration, the spatial discretization needs to provide additional regularization [3], we use the 3rd order ENO scheme of Section 2.2.

3. SHOCK–WAVE INTERACTION WITH SOLENOIDAL VELOCITY FLUCTUATIONS

We apply the procedures outlined in Section 2 to a generic two-dimensional test problem for shock–turbulence interaction, as suggested by Shu and Osher [19]. A correct computation of wave amplification across a shock is a requirement for any subgrid-scale model to be applicable for shock–turbulence interaction. Also, since a shock is a subgrid scale, a sufficiently general subgrid-scale model should provide a proper filtered shock solution. We solve the two-dimensional Euler equations (Equation (1)) with the fluxes (Equation (5)) on the domain $(t; x, y) \in [0, \infty) \times [-1.5, 1.5] \times [-1, 1]$. The initial conditions constitute a $M = 8$ shock moving into an oblique divergence-free vorticity-fluctuation field. From shock relations (e.g. Thompson [24]) the shock propagation velocity is

$$\bar{u} = MC_{s1}$$

where C_s is the speed of sound (we denote with '1' the pre-shock state and with '2' the post-shock state). The initial pre-shock state ($x \geqslant 1$) is

$$
\begin{aligned}
u(x, y) &:= -C_{s1} \sin\theta \cos(xk \cos\theta + yk \sin\theta) \\
v(x, y) &:= C_{s1} \cos\theta \cos(xk \cos\theta + yk \sin\theta) \\
\rho(x, y) &:= 1 \\
p(x, y) &:= 1
\end{aligned}
$$

with the parameters $\theta = \pi/6$, $k = 2\pi$, while the corresponding initial post-shock state ($x < 1$) is

$$
\begin{aligned}
u(x, y) &:= \frac{2 + (\kappa - 1)M^2}{(\kappa + 1)M^2} u_1 \\
v(x, y) &:= 0 \\
\rho(x, y) &:= \frac{(\kappa + 1)M^2}{2 + (\kappa - 1)M^2} \rho_1 \\
p(x, y) = p_2 &:= \left(1 + \frac{2\kappa}{\kappa + 1}(M^2 - 1)\right)
\end{aligned}
$$

Thus $C_{s1} = \sqrt{\kappa}$, where κ has been set to 1.4.

Boundary conditions are imposed in terms of Riemann variables, which are prescribed along characteristics pointing into the computational domain in terms of the Riemann variables along outward pointing characteristics. In all cases $CFL = 0.5$ is used and the time step is estimated by

$$
\tau = CFL \left[\max_{\mathscr{D}} \left(\frac{u}{h_x}, \frac{u - C_s}{h_x}, \frac{u + C_s}{h_x} \right) + \max_{\mathscr{D}} \left(\frac{v}{h_y}, \frac{v - C_s}{h_y}, \frac{v + C_s}{h_y} \right) + \chi \right]^{-1}
$$

where for DDM χ is used according to Equation (13), for the other cases $\chi = 0$.

For computations with DDM we have chosen $\chi = 1/2 + 60/h$, which was found to be suitable for the Euler equations in one-dimensional tests for the isothermal 'slow-shock problem' and for the shock-interaction with an entropy fluctuation [2]. Another set of computations was performed with $\chi = 1 + 120/h$ to confirm the weak dependence of the results on the relaxation parameter χ. For time integration the 3rd order TVD Runge–Kutta scheme of Shu [18] was used. We also have tested the low-storage Runge–Kutta scheme of Wiliamsson [26] and found no change of the results.

We compare filtered and resolved pressure distributions for $N_x = 60$ and $N_y = 40$ and $N_x = 120$, $N_y = 80$, respectively, obtained with the different approaches of Section 2, shown in Figures 3, 4 and 5, 6, with a well resolved ENO computation with $N_x = 480$, $N_y = 240$ points in Figure 11. We note that the DDM approach gives a good resolution of the pressure disturbance passing through the shock. The DSM approach shows the shock representation being affected by the model, also the passage of the disturbance through the shock is less accurately predicted than with the other models. Similar observations can be made for the vorticity distribution $\omega = \partial_y u - \partial_x v$ shown in Figures 7, 8 and 9, 10.

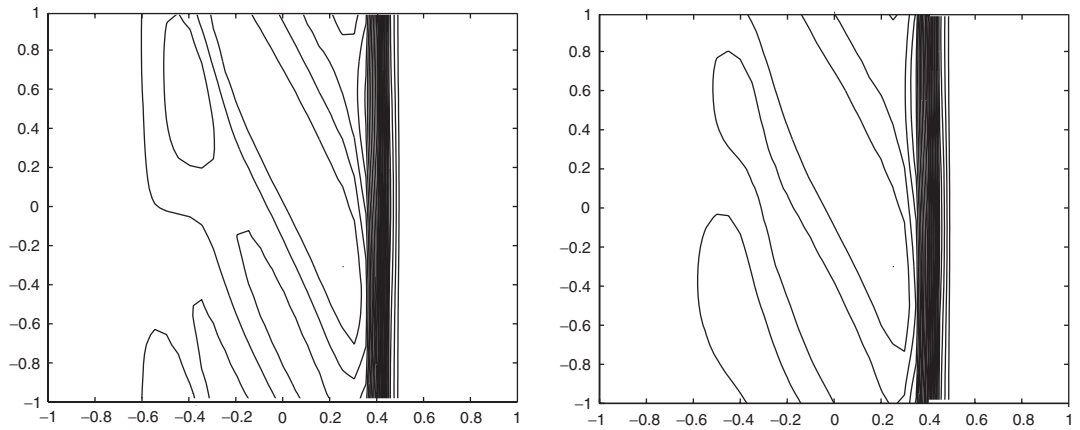

(a) MILES (b) DSM

Figure 3. Pressure p, $N_x = 60$, $N_y = 40$; 29 contours $1 \leqslant p \leqslant 80$.

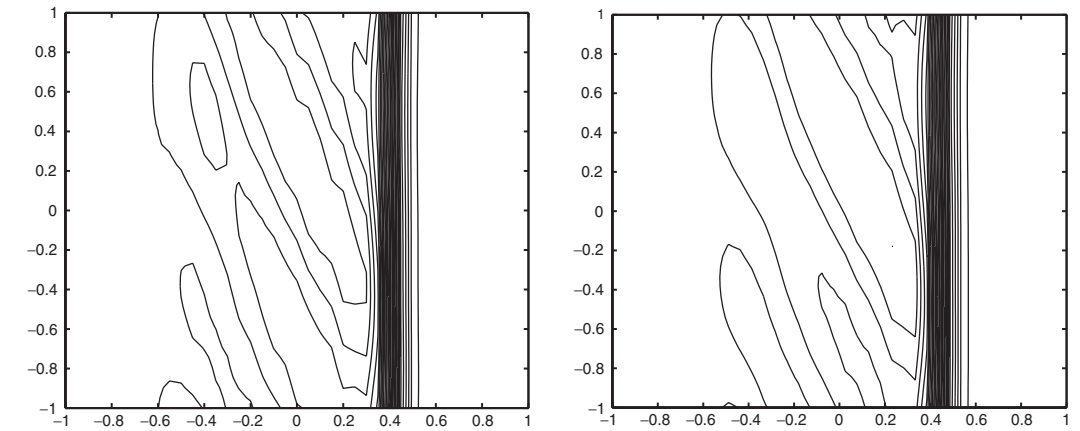

(a) DDM, $\chi = 1/2 + 60/h$ (b) DDM, $\chi = 1 + 120/h$

Figure 4. Pressure p, $N_x = 60$, $N_y = 40$; 29 contours $1 \leqslant p \leqslant 80$.

Setting the relaxation parameter of DDM to a twice larger value has only a weak effect on the results, Figures 3 and 6. A closer look at the post-shock density disturbances which are generated by the solenoidal wave due to its interaction with the shock in Figure 12 shows that the deconvolution approach exhibits the best wave resolution, although the primary-filtered shock representation is less sharp than the formally unfiltered representation in the MILES approach. It should be noted that for MILES and DSM it is difficult to define a proper filtered reference solution since the implicitly assumed grid filter is a result of the spatial discretization. Formally, DSM should return a filtered solution, where for the filtering the primary filter of the DDM method is used (as test filter the same with twice the filter width). We note that the shock is represented similarly sharp as with MILES (the shock resolution may however

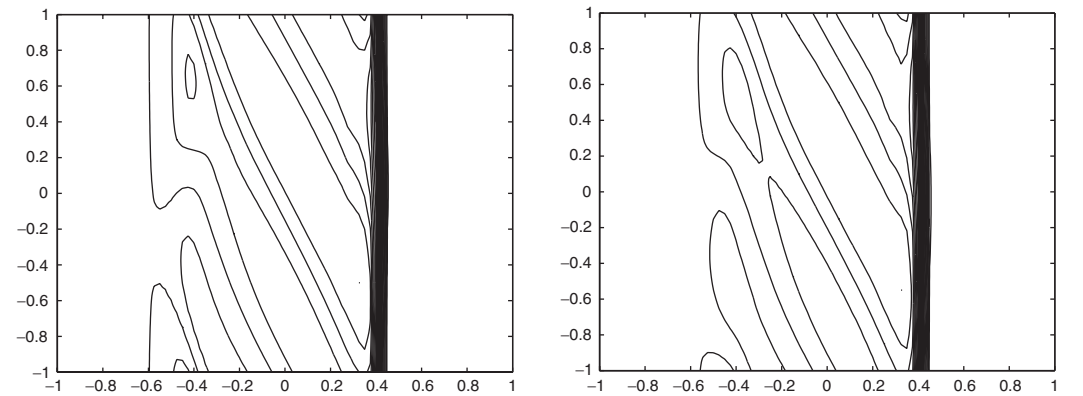

Figure 5. Pressure p, $N_x = 120$, $N_y = 80$; 29 contours $1 \leqslant p \leqslant 80$.

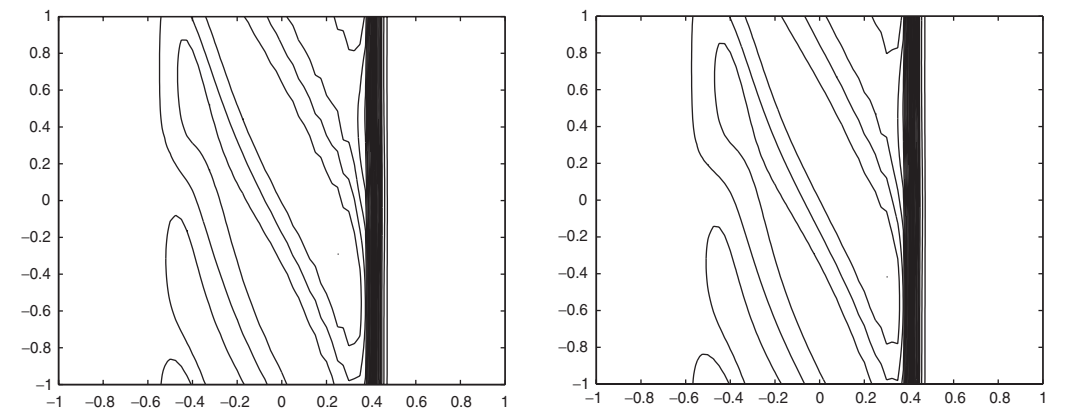

Figure 6. Pressure p, $N_x = 120$, $N_y = 80$; 29 contours $1 \leqslant p \leqslant 80$.

be affected by the clipping of the dynamic Smagorinsky parameter) but that the amplitude of the generated density wave is underpredicted. We also find that the DSM approach with ENO as the underlying discretization requires more than twice as much CPU time as the DDM approach, where the DDM approach could be made more efficient by integrating the stiff linear relaxation term implicitly. DSM with a central scheme is unstable.

4. CONCLUSIONS

The explicit use of filtering and de-filtering has considerably improved the prediction capabilities of subgrid-scale modelling in LES [1]. For shock-capturing, filtering is mostly based on non-linear approaches [11, 27], where regularization is achieved by limiters or ENO-type

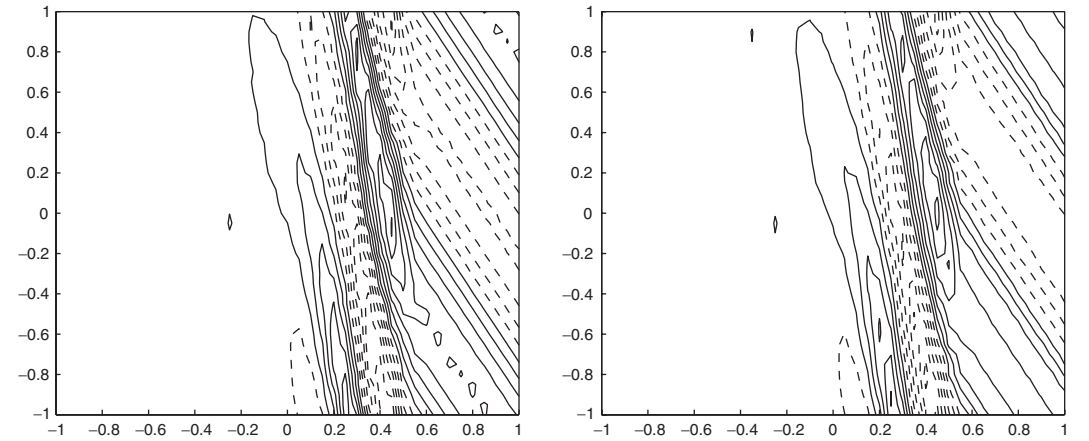

(a) MILES (b) DSM

Figure 7. Vorticity ω, $N_x = 60$, $N_y = 40$; 15 contours $-13 \leqslant \omega \leqslant 13$, —— $\omega \geqslant 0$, - - - - $\omega < 0$.

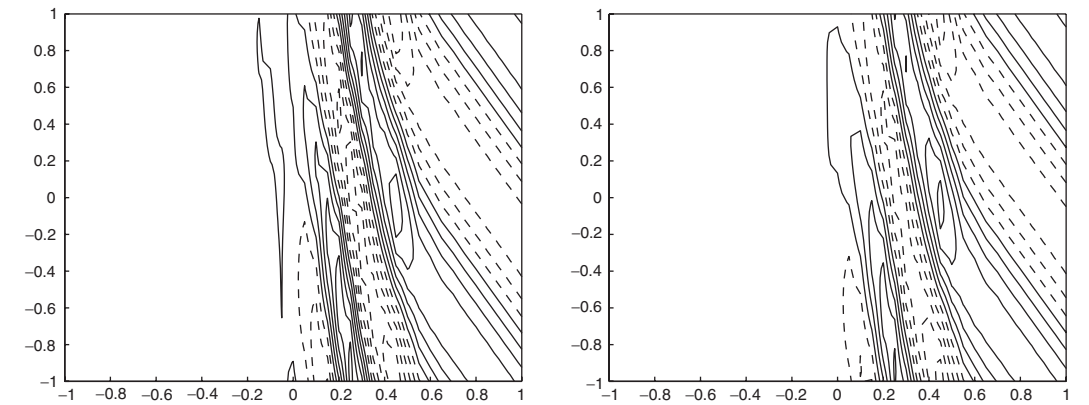

(a) DDM, $\chi = 1/2 + 60/h$ (b) DDM, $\chi = 1 + 120/h$

Figure 8. Vorticity ω, $N_x = 60$, $N_y = 40$; 15 contours $-13 \leqslant \omega \leqslant 13$, —— $\omega \geqslant 0$, - - - - $\omega < 0$.

stencil switching. The spectral viscosity method of Tadmor [23] allows for an accurate representation of discontinuous solutions with a linear algorithm, involving, however, a dual-space representation of the solution. We have presented a recently proposed deconvolution approach with a real-space regularization [2] resembling a spectral-viscosity, and we have applied this approach to a generic test case for shock–turbulence interaction. The results for the deconvolution method are in good agreement with filtered shock solutions and provide a better small-scale resolution than the other models.

Formally, in LES filtered equations are solved, such that the shock which is a non-turbulent subgrid scale should be represented as filtered shock. Since traditional subgrid-scale models are not suited for capturing shocks they are often supplemented with shock-capturing methods for

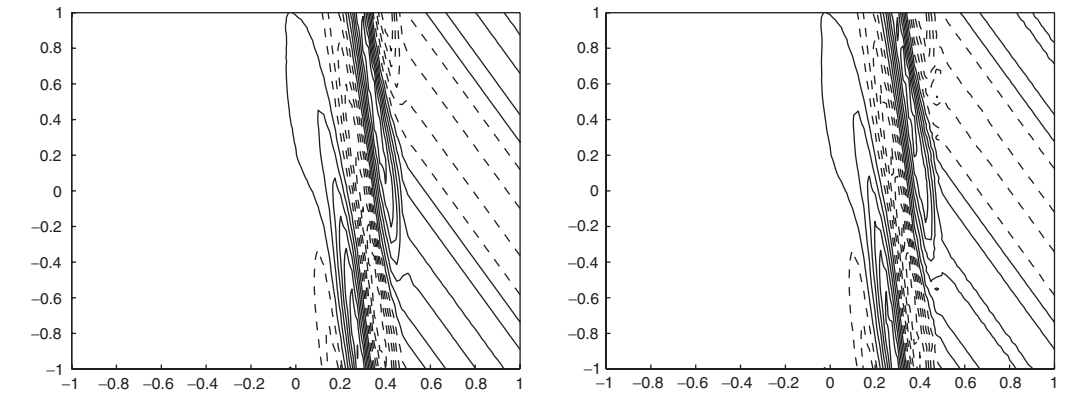

(a) MILES (b) DSM

Figure 9. Vorticity ω, $N_x = 120$, $N_y = 80$; 15 contours $-24 \leqslant \omega \leqslant 24$, —— $\omega \geqslant 0$, - - - - $\omega < 0$.

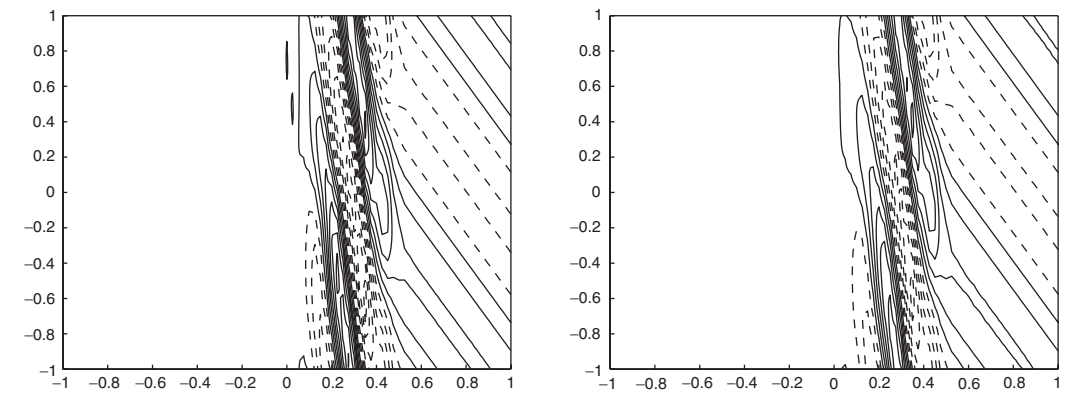

(a) DDM, $\chi = 1/2 + 60/h$ (b) DDM, $\chi = 1 + 120/h$

Figure 10. Vorticity ω, $N_x = 120$, $N_y = 80$; 15 contours $-24 \leqslant \omega \leqslant 24$, —— $\omega \geqslant 0$, - - - - $\omega < 0$.

stable integration, see Section 2.3. This procedure may result in a sharper shock representation than that corresponding to the assumed grid filter, thus being formally inconsistent with the LES equations. In applications of LES for shock–turbulence interaction one should expect a shock width corresponding to the filtered exact shock solution at best.

Since the deconvolution approach shares a considerable degree of commonality with recent deconvolution models for subgrid-scale modelling for LES [20–22] we expect that it will prove useful for the LES of shock–turbulence interaction. We believe that the significance of numerical-entropy regularizations for subgrid-scale modelling requires further investigation. The results quoted by Jiménez and Moser [10], Jiménez [9] seem to indicate that the restriction of the solution domain by the primary filter may result in a loss of uniqueness of the subgrid-scale model. It can also be suspected that solutions with energy equipartition which are commonly observed for spectral discretizations of the three-dimensional Euler equations

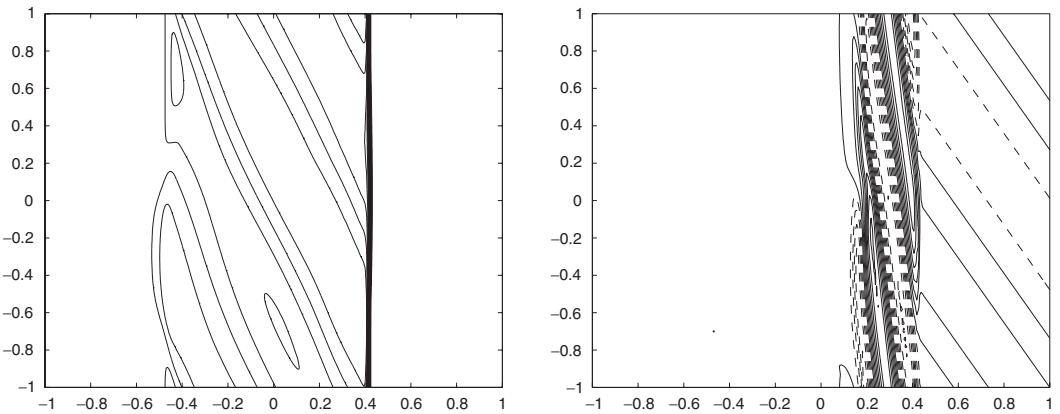

(a) Pressure $1 \le p \le 80$, 29 contours. (b) Vorticity $-38 \le \omega \le 38$, 15 contours

Figure 11. ENO, $N_x = 480$, $N_y = 240$.

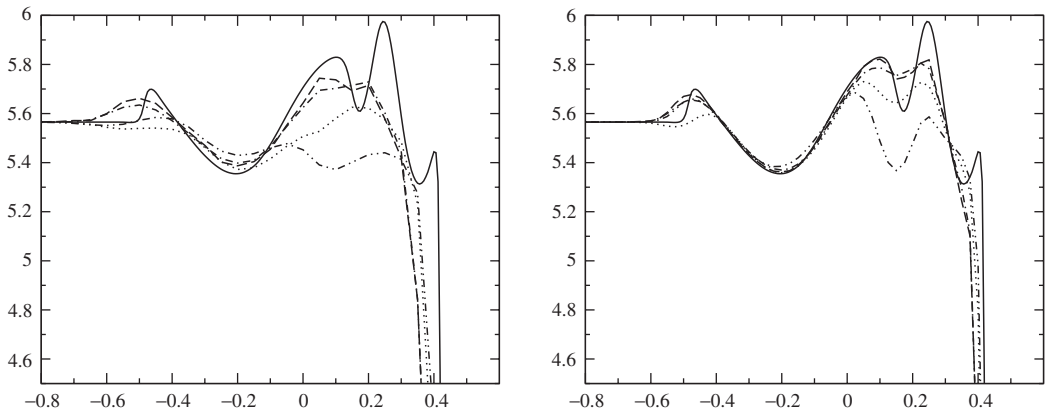

(a) $N_x = 60$, $N_y = 40$ (a) $N_x = 120$, $N_y = 80$

Figure 12. Density at $y = 0$, · · · · · · · MILES, - - - - DDM with $\chi = 1/2 + 60/h$, – · – DDM with $\chi = 1 + 120/h$, — ·· — DSM, —— high-resolution ENO.

correspond to improper weak solutions of non-regularized numerical discretizations of conservation laws and thus are mere artifacts of the discrete system.

ACKNOWLEDGEMENTS

The author wishes to acknowledge stimulating and helpful discussions during the work, part of which is presented in this paper, with A. Leonard (CalTech, Pasadena), P. Moin (CTR, Stanford), L. Kleiser (ETH Zürich), S. Stolz (ETH Zürich), D. Pruett (JMU, Harrisonburg), A. Domaradzki (USC, Los Angeles).

REFERENCES

1. Adams NA, Stolz S. Deconvolution methods for subgrid-scale approximation in large-eddy simulation. In B. Geurts (ed.), *Modern Simulation Strategies for Turbulent Flow*. R. T. Edwards, 2001; 21–41.
2. Adams NA, Stolz S. A Subgrid-scale Deconvolution Approach for Shock Capturing. *Journal of Computational Physics* 2002; at press.
3. Adams NA, Stolz S, Honein A, Mahesh K. Analysis and subgrid modelling of shock-wave/boundary-layer interaction. In *CTR Proc. 1998 Summer Program*, Stanford, California, 1998. Center for Turbulence Research, Stanford University and NASA Ames Research Center.
4. Boris JP, Grinstein FF, Oran ES, Kolbe RL. New insights into large eddy simulation. In *Fluid Dynamics Research* 1992; **10**:199–228.
5. Ducros F, Ferrand V, Nicoud F, Weber C, Darracq D, Gacherieu C, Poinsot T. Large-eddy simulation of the shock turbulence interaction. *Journal of Computational Physics* 1999; **152**(2):517–549.
6. Garnier E, Mossi M, Sagaut P, Comte P, Deville M. On the use of shock-capturing schemes for large-eddy simulation. *Journal of Computational Physics* 1999; **153**:273–311.
7. Gustafsson B, Kreiss H-O, Oliger J. *Time Dependent Problems and Difference Methods*. John Wiley & Sons: New York, 1995.
8. Jameson A, Schmidt W, Turkel E. *Numerical solutions of the Euler equations by finite volume methods using Runge–Kutta time stepping*, vol. 81–1259, 1981.
9. Jiménez J. Limits and performance of eddy viscosity sub-grid models. In P. Voke, N. D. Sandham, L. Kleiser (eds), *Direct and Large-Eddy Simulation III*. Kluwer, 1999; 75–86.
10. Jiménez J, Moser RD. Large-eddy simulations: where are we and what can we expect. *AIAA Journal* 2000; **38**:605–612.
11. Lafon F, Osher S. High order filtering methods for approximating hyperbolic systems of conservation laws. *Journal of Computational Physics* 1991; **96**:110–142.
12. Lele SK. Compact finite difference schemes with spectral-like resolution. *Journal of Computational Physics* 1992; **103**:16–42.
13. Lesieur M. *Turbulence in Fluids*. Kluwer Academic Publishers: Dordrecht, The Netherlands, 3rd edition, 1997.
14. Moin P, Squires K, Cabot W, Lee S. A dynamic subgrid-scale model for compressible turbulence and scalar transport. *The Physics of Fluids A* 1991; **3**:2746–2757.
15. Pruett CD, Adams NA. A priori analyses of three subgrid-scale models for one-parameter families of filters. *The Physics of Fluids* 2000; **12**:1133–1142.
16. Richtmyer RD, Morton KW. *Difference Methods for Initial-Value Problems*. John Wiley & Sons: New York, 2nd edition, 1965.
17. Roe PL. Characteristic-based schemes for the Euler equations. *Annual Review of Fluid Mechanics* 1986; **18**:337–365.
18. Shu C-W. Total-variation-diminishing time discretizations. *SIAM Journal on Scientific and Statistical Computing* 1988; **9**(6):1073–1084.
19. Shu C-W, Osher S. Efficient implementation of essentially non-oscillatory shock-capturing schemes, II. *Journal of Computational Physics* 1989; **83**:32–78.
20. Stolz S, Adams NA. An approximate deconvolution procedure for large-eddy simulation. *The Physics of Fluids* 1999; **11**:1699–1701.
21. Stolz S, Adams NA, Kleiser L. An approximate deconvolution model for large-eddy simulation with application to incompressible wall-bounded flows. *The Physics of Fluids* 2001; **13**:997–1015.
22. Stolz S, Adams NA, Kleiser L. The approximate deconvolution model for LES of compressible flows and its application to shock-turbulent-boundary-layer interaction. *The Physics of Fluids* 2001; **13**:2985–3001.
23. Tadmor E. Convergence of spectral methods for non-linear conservation laws. *SIAM Journal on Numerical Analysis* 1989; **26**:30–44.
24. Thompson PA. *Compressible-Fluid Dynamics*. Advanced Engineering Series. Rensselaer Polytechnic Institute, 1988.
25. Vreman B. *Direct and Large-Eddy Simulation of the compressible turbulent mixing layer*. PhD thesis, University of Twente, 1995.
26. Williamson JH. Low-storage Runge–Kutta schemes. *Journal of Computational Physics* 1980; **35**:48–56.
27. Yee HC, Sandham ND, Djomehri MJ. Low-dissipative high-order shock-capturing methods using characteristic-based filters. *Journal of Computational Physics* 1999; **150**:199–238.

